This is an open access article published under a Creative Commons Non-Commercial No Derivative Works (CC-BY-NC-ND) Attribution License, which permits copying and redistribution of the article, and creation of adaptations, all for non-commercial purposes.

ACS AUTHORCHOICE

ACS OMEGA

http://pubs.acs.org/journal/acsodf

Article

Origins of Optical Activity in an Oxo-Helicene: Experimental and Computational Studies

Taye B. Demissie,* M. Shyam Sundar, Karthick Thangavel, Valery Andrushchenko,* Ashutosh V. Bedekar, and Petr Bouř*

Cite This: *ACS Omega* 2021, 6, 2420−2428

Read Online

ACCESS | Metrics & More | Article Recommendations | Supporting Information

ABSTRACT: Helicenes are known to provide extremely strong optical activity. Prediction of the properties of helicenes may facilitate their design and synthesis for analytical or materials sciences. On a model 7,12,17-trioxa[11]helicene molecule, experimental results from multiple spectroscopic techniques are analyzed on the basis of density functional theory (DFT) simulations to test computational methodology and analyze the origins of chirality. Infrared (IR), vibrational circular dichroism (VCD), electronic circular dichroism (ECD), magnetic circular dichroism (MCD), and Raman optical activity (ROA, computations only) spectra are compared. Large dissymmetry factors are predicted both for vibrational (ROA/Raman ∼ VCD/IR ∼ 10^{-3}) and electronic (ECD/Abs ∼10^{-2}) optical activity, which could be verified experimentally except for ROA. Largest VCD signals come from a strong vibrational coupling of the C−H in-plane and out-of-plane bending modes in stacked helicene rings. The sum-over-states (SOS) approach appeared convenient for simulation of MCD spectra. Our results demonstrated that selected computational methods can be successfully used for reliable modeling of spectral and chiroptical properties of large helicenes. In particular, they can be used for guiding rational design of strongly chiral chromophores.

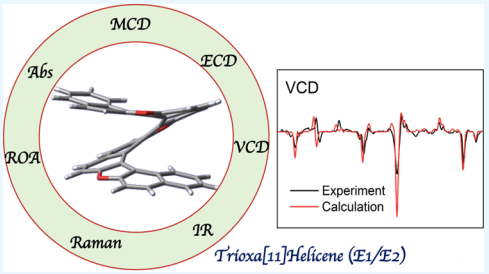

INTRODUCTION

Helicenes are polycyclic aromatic molecules with benzene rings forming a helix.[1,2] Helicenes are usually thermally stable because of the stabilizing effect of the π−electron conjugation.[3−9] Nevertheless, they are sometimes also referred to as "molecules in distress"[10] because of the distorted aromatic system.[1] Even without chiral centers or asymmetric chromophores, they may form stable enantiomers and exhibit optical activity due to the helical structure. Particularly strong are their electronic circular dichroism (ECD) spectra owing to the electron conjugation. Helicenes have attracted wide attention in material science because of their extraordinary physical and chiroptical properties.[11] Potential applications include molecular recognition, molecular machines, chemosensing, catalysis, organic light-emitting diodes, and organic field-effect transistors.[1,2,12−15]

Even though the first helicenes were reported 100 years ago, their chemistry and properties are not fully understood.[1,12,13] For example, questions about their biological activity (or toxicity) have appeared recently.[1,12,13] Their chiroptical and chemical properties have been shown to be important for many applications including asymmetric synthesis, liquid crystal displays, molecular switches and machines, or stereoselective catalysis.[1,12,13] Heterohelicenes, such as those incorporating oxygen or nitrogen atoms, can provide additional functionalities, exhibiting broader, enhanced, and more diverse applications compared to their carbohelicene counterparts.[2,8,9,16]

Helicenes and their derivatives have thus been extensively studied with different chiroptical spectroscopic techniques. However, such studies were often limited to relatively small [*n*]helicenes (with n = 4 to 6) and involved mainly optical rotation (OR) and ECD spectroscopy.[17−20] Smaller molecules were also studied theoretically using time-dependent density functional theory (TD-DFT). For instance, the ECD spectra of [7]heterohelicene[16] and diaza-embedded [4]helicenes and pseudo[4]helicenes[11] were explained by DFT. Later, calculations were performed for few larger helicenes with n = 12 and 16.[18,21]

However, in the last decades, rather novel chiroptical methods, such as vibrational circular dichroism (VCD), Raman optical activity (ROA), and circularly polarized luminescence (CPL), allowed exploration of the geometric and electronic structures more extensively.[22,23] The VCD and ROA spectra may provide additional information related to

Received: December 14, 2020
Accepted: December 24, 2020
Published: January 7, 2021

Downloaded via ACADEMY OF SCIENCES CZECH REPUBLIC on February 22, 2021 at 12:40:07 (UTC).
See https://pubs.acs.org/sharingguidelines for options on how to legitimately share published articles.

ACS Publications

© 2021 The Authors. Published by American Chemical Society

chirality and redox switching; for example, they revealed how molecular vibrational modes are modified upon oxidation.[22−29]

In this study, we explored the chiroptical properties of a large oxygen-containing 7,12,17-trioxa[11]helicene ("trioxa[11]helicene"). The synthesis and X-ray structure of this compound were reported earlier.[30] The molecule makes about one-and-a-half turn of the helix about 10.2 Å in diameter, resulting in significant delocalization of π electrons (Figure 1). Stable enantiomers were confirmed by HPLC analysis, and the molecule was proposed as a promising component for materials science.[30] Furthermore, its trioxa-skeleton is easy to prepare and modify, and it can serve as a starting point for derivatives with varied properties. At the same time, the size of the molecule still allows for thorough theoretical investigation, which could assist in rational design of further derivatives with advanced properties.

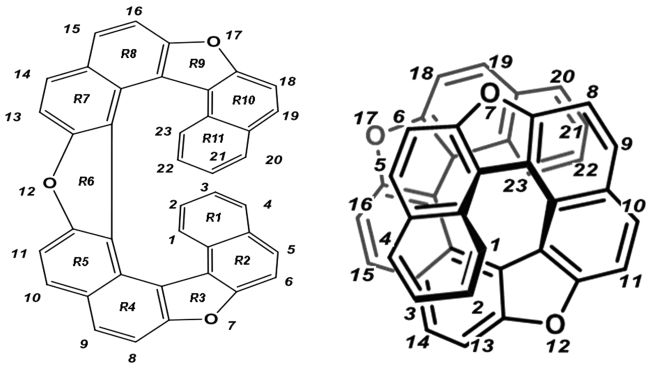

Figure 1. Chemical structure, ring numbering, and atom numbering of 7,12,17-trioxa[11]helicene.

In addition to ECD and VCD spectroscopy, we also utilized magnetic circular dichroism (MCD), which was proposed as a powerful technique to study aromatic molecules.[31−35] ROA spectra could be only calculated but not measured due to strong sample fluorescence. Overall, we find the combined experimental/theoretical approach particularly beneficial in understanding and rationalizing helicene chiroptical properties.

It was pointed out earlier that theoretical methods applicable for small molecules may fail for larger helicenes due to long-range conjugation and charge transfer effects.[36] Therefore, the confrontation of experimental and theoretical data is also important from the point of further development of the computational methodology.

RESULTS AND DISCUSSION

Geometry. Selected structural parameters are compared with X-ray data in Table 1. The molecule has C_2 symmetry. The predicted structural parameters at the B3LYP/6-311++G**/PCM(THF) level of approximation well reproduce the experimental ones. For example, the dihedral angle between the five-membered rings (experimentally −23.7°) is nicely reproduced by B3LYP (−23.3°), while ωB97X-D underestimates it by 3.1° (−20.6°). B3LYP slightly overestimated the relevant nonbonding distances (with an error for r_1 = 0.185 Å and for r_2 = 0.122 Å), whereas ωB97X-D slightly underestimated them (with an error for r_1 = −0.217 Å and for r_2 = −0.272 Å).

The differences in the nonbonding distances found between the crystal and theoretical values were only 3.4 and 1.5% for r_1 and r_2, respectively, using B3LYP; while both differences were 3.4% for the ωB97X-D level of calculation. Nevertheless, the geometrical parameters were overall satisfactorily reproduced by both functionals, with accuracy consistent with previous studies of unsubstituted and substituted carbo[n]helicene derivatives.[29,37,38]

Table 1. Selected Experimental and Calculated Structural Parameters of Trioxa[11]helicene

coordinate	experimental	B3LYP	error	ωB97X-D	error
bond length (Å)					
C−O	1.367	1.368	−0.001	1.361	0.006
C′−O	1.371	1.368	0.003	1.361	0.010
C−C (inner)[a]	1.432	1.433	−0.001	1.426	0.006
C−C (inner)[b]	1.452	1.461	−0.009	1.455	−0.003
C−C (inner)[c]	1.409	1.416	−0.007	1.413	−0.004
C−C (outer)[d]	1.393	1.398	−0.005	1.399	−0.006
C−C (outer)[e]	1.352	1.375	−0.023	1.367	−0.015
C−C (outer)[f]	1.416	1.425	−0.009	1.424	−0.008
angle (degree)					
∠OO′O	42.8	42.2	0.6	40.3	2.5
∠OOO′	68.3	68.9	−0.6	69.9	−1.6
∠CCCC (5mr)	−7.1	−7.3	0.2	−7.1	0.0
∠CCCC (5-to-5)	−23.7	−23.3	−0.4	−20.6	−3.1
nonbonding (Å)					
A	10.030	10.130	−0.100	10.240	−0.210
r_1	5.466	5.868	0.185	5.651	−0.217
r_2	7.905	8.299	0.122	8.027	−0.272

[a]C−C bonds at the inner part and one bond far from the five-membered rings. [b]C−C bonds at the inner part and part of the five-membered ring. [c]C−C bonds at the inner part of the last six-membered ring. [d]C−C bonds at the outer part and one bond far from the five-membered rings. [e]C−C bonds at the outer part and part of the six-membered rings. [f]C−C bonds at the outer part and three bonds far from the five-membered rings, A: the distance between hydrogen atoms at a nearly 180° orientation; r_1: C(1)−C(23) nonbonding distance; r_2: C(2)−C(22) nonbonding distance. Note that this numbering only considers the H−C and O atoms. Error = experimental − calculated.

Absorption and Electronic Circular Dichroism. The experimental and calculated (B3LYP) absorption spectra of trioxa[11]helicene are presented in Figure 2. The ωB97X-D results, which display slightly worse agreement with the experiment, are shown in the Supporting Information (SI). This poorer agreement of the ωB97X-D spectra correlates with the generally larger deviations of the ωB97X-D-calculated geometry from the experimental one, as mentioned above. The B3LYP computation reproduces the experimental spectral features quite well, with a typical wavelength error of ∼20 nm and intensity error within 0−50%. This is supported by the high value of the similarity overlap between the computed and experimental absorption spectra (*Sim*UV = 0.89, Table S1 of SI). The spectral band assignments are listed in Table 2. Among these assignments, band I (418.9 nm) is dominated by the HOMO−LUMO transition (the molecular orbitals (MOs) are delocalized within the entire molecule, Figure 2), whereas band IV (368.0 nm) is mainly a transition from HOMO to

https://dx.doi.org/10.1021/acsomega.0c06079
ACS Omega 2021, 6, 2420−2428

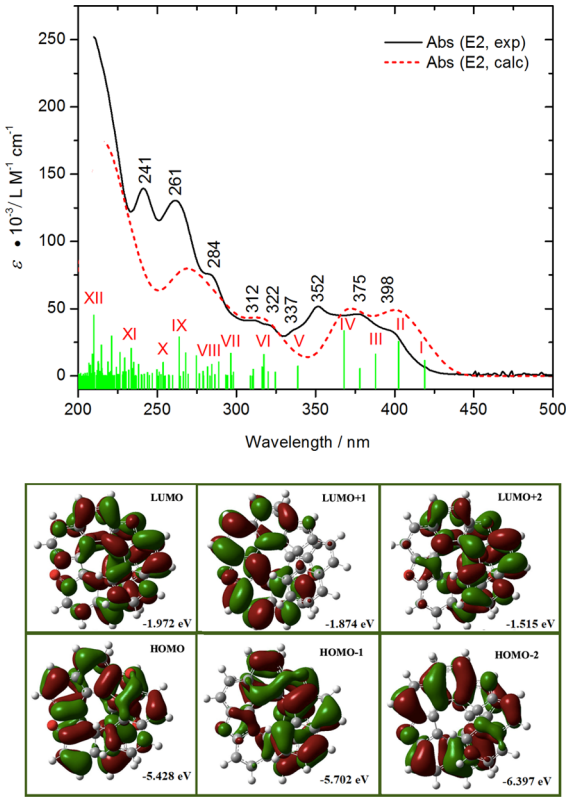

Figure 2. Comparison of the experimental (measured in THF) and calculated (B3LYP/PCM(THF)) absorption spectra (top). Black Arabic numbers show experimental peak positions, red Roman numerals correspond to the calculated band assignment in Table 2, vertical green lines indicate relative transition intensities and positions. Frontier molecular orbitals and energies (B3LYP/6-311++G**/PCM(THF)) (bottom).

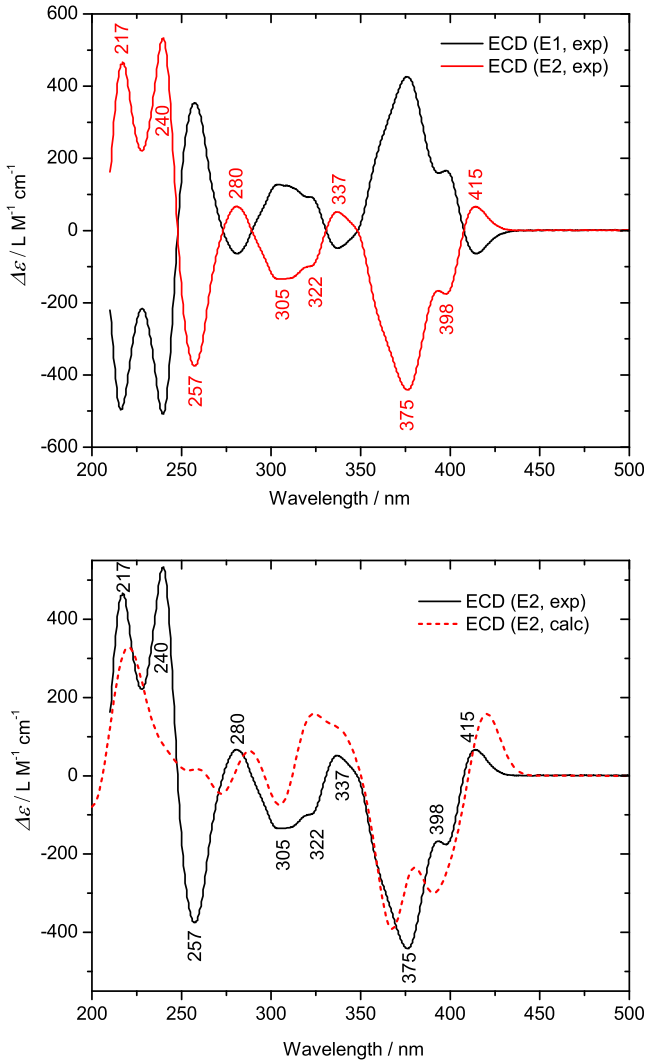

Figure 3. Experimental ECD spectra (measured in THF) of E1 and E2 enantiomers (top) and experimental and calculated (B3LYP/PCM(THF)) ECD spectra of E2 (bottom). The peak positions relate to the experiment.

LUMO + 2 and has the second largest transition dipole moment (6.66 D, see Table 2).

The ECD spectra are plotted in Figure 3. Experimentally, strong bisignate negative and positive Cotton effects are observed at around 217, 240, 257, 305, and 375 nm. Other peaks are around 280, 337, and 415 nm, and shoulders are around 322 and 398 nm. The two enantiomers provide nearly "mirror image" spectra, confirming reliability of the experiment. The maximal electronic dissymmetry factor (EDF) reaches 10^{-2} (e.g., for the transition around 375 nm, see Figure

Table 2. Strongest Lowest-Energy Electronic Transitions in Trioxa[11]helicene, Wavelength (λ, in nm), Oscillator Strength (f), Transition Electric Dipole Moments (μ, in debyes), Dominant MOs, and Symmetry (TD-B3LYP/6-311++G/PCM(THF) Calculation)**

band	excitation #	λ (nm)	F	μ	dominant MOs	symmetry
I	1	418.9	0.0660	2.31	142 → 143[a] (94%)	A
II	2	402.5	0.1514	5.10	142 → 144 (90%)	B
III	3	387.8	0.0990	3.21	141 → 143 (95%)	B
IV	5	368.0	0.2163	6.66	142 → 145 (87%)	B
V	6	338.8	0.0522	1.48	141 → 145 (91%)	A
VI	9	317.3	0.1202	3.19	140 → 143 (45%), 142 → 146 (34%)	B
VII	16	296.5	0.1353	3.36	138 → 144 (39%), 141 → 147 (25%)	B
VIII	21	284.5	0.0722	1.72	142 → 150 (33%), 141 → 149 (23%)	A
IX	29	268.0	0.1530	3.43	141 → 149 (16%), 142 → 148 (14%), 136 → 134 (12%)	A
X	38	253.7	0.0945	2.01	142 → 153 (27%), 136 → 145 (20%), 137 → 145 (17%)	A
XI	65	229.5	0.1396	2.68	142 → 162 (34%), 138 → 149 (17%), 139 → 149 (10%)	B
XII	104	210.0	0.5086	8.93	135 → 148 (12%), 134 → 147 (10%), 135 → 147 (10%)	A

[a]Molecular orbital 142 is the highest occupied molecular orbital (HOMO), whereas 143 is the lowest unoccupied molecular orbital (LUMO).

https://dx.doi.org/10.1021/acsomega.0c06079
ACS Omega 2021, 6, 2420−2428

S1 of SI), and the molecule is thus a good example of helicenes exhibiting strong chirality. There is a reasonable agreement between the calculated and experimental ECD curves, in particular at the higher wavelength region, although the typical error is larger than for the absorption, which is reflected in the lower similarity overlap *Sim*ECD = 0.41 (Table S1). The experimental ECD bands at 415, 398, 375, 337, and 280 nm are well reproduced by the calculations, which allows verification of the assignment of the absorption transitions I, II, IV, V, and VIII, respectively. A good agreement for these transitions is confirmed by a comparison of the corresponding bands in the calculated and experimental EDF spectra (Figure S1). The overall similarity overlap for EDF spectra *Sim*EDF is 0.60, which is in between of the values for *Sim*UV and *Sim*ECD (Table S1). The broad composite experimental ECD feature around 305−322 nm, originating from the absorption band at 312−322 nm, is only partially reproduced by the calculations as a relatively narrow band at 305 nm. Most probably, it could be assigned to the absorption band VI. The shortest-wavelength ECD band at 217 nm is well reproduced and can be assigned to the absorption transition XII (see also Figure S1). However, the experimental couplet at 240(+)/257(−) nm is calculated with a much lower intensity, which is also clearly visible in the EDF spectra (Figure S1). A worse agreement in this region can be explained by the high density of electronic states and the usual DFT error.[39]

Magnetic Circular Dichroism. The experimental and calculated MCD spectra are presented in Figure 4. The

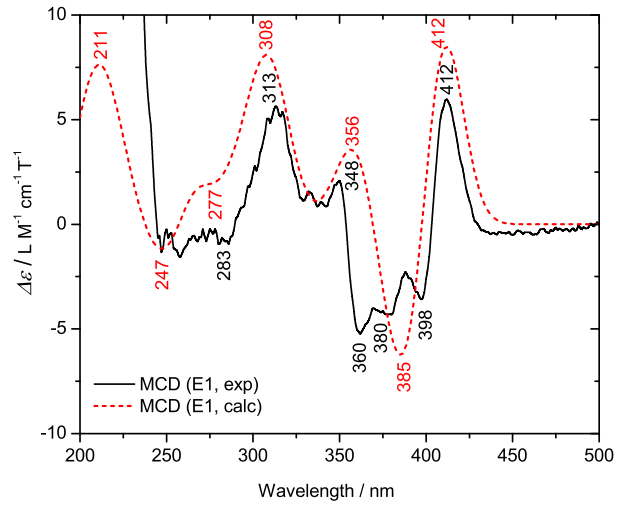

Figure 4. Experimental (measured in THF) and calculated (B3LYP/PCM(THF)) MCD spectra. Black numbers show peak positions for the experiment, and red numbers relate to the calculated spectrum.

calculation (B3LYP/6-311++G**/PCM) reproduces the experiment (both intensities and band positions) reasonably well (with similarity overlap *Sim*MCD = 0.37, Table S1). The observed MCD band at 412 nm ($\Delta\varepsilon$ = 6 L·M^{-1}·cm^{-1}·T^{-1}) corresponds to the absorption peak at 418.9 nm, originating in a transition between HOMO and LUMO. This transition is also active in ECD and shows a band at 415 nm (Figure 3). The spectral range within 360−400 nm (absorption bands II, III, and IV), showing only two bands in ECD (at 375 and 398 nm), is better resolved in MCD, producing a clear splitting into three bands at 360, 380, and 398 nm. While this splitting is clearly documented by the calculated absorption spectrum (Figure 2 and Table 1), the calculated MCD shows only a single narrow band at 385 nm. The other major MCD bands (observed at 348, 313, and 283 nm) are correctly calculated with very close positions and band shape, which is confirmed by fairly good agreement between magnetic dissymmetry factor (MDF) spectra (Figure S2) with *Sim*MDF = 0.48 (Table S1). While the experimental signal could not be measured below 250 nm due to strong absorption, the calculations provide us an insight into this spectral range, suggesting the presence of two MCD bands with the opposite sign, at 247 and 211 nm, originating from the transitions X and XII, respectively. The high-intensity MCD bands at 313 and 412 nm originate from the dominant $\pi-\pi^*$ transitions, as usual for helicenes.[40] Most of the transitions are localized at the stacked region of the aromatic parts (Figure 2).

Although the ωB97X-D functional is technically more advanced by including dispersion correction,[41] the dispersion did not seem to be critical when modeling the spectra of single molecules.[42] This has also been cross-checked using B3LYP-GD3 (see Figures S4 and S5).

Vibrational Circular Dichroism. Earlier VCD investigation of heptahelicene ([7]helicene) by Bürgi *et al.*[26] found that the intramolecular repulsive force between the ends of the helix provides pronounced rigidity to the molecule. The helical structure of trioxa[11]helicene is also characterized by the repulsive forces between the carbon atoms, which makes an interplanar angle of 24.37° between the intersections passing through the ring R1−R9. In agreement with the study by Bürgi *et al.*,[26] there are repulsive $\pi-\pi$ stacking interactions between the overlying rings (R1/R8, R2/R9, R3/R10, R4/R11) at the ends of the helix. Miyasaka and co-workers[43] predicted that the helical folding is driven by intermolecular π-stacking and steric repulsive interactions. Similarly, strong intermolecular $\pi-\pi$ stacking interactions were observed in the crystal packing of pyrene-fused double [7]carbohelicene.[9] The $\pi-\pi$ stacking interactions in trioxa[11]helicene are also supported by the Mülliken atomic charge analysis of the carbon atoms of the overlying rings. For instance, the total atomic charge on C2 and C3 of R1 are −0.459 and −0.528, respectively; whereas those on C15 and C16 of R8, respectively, are −0.057 and −0.456, implying that these carbon atoms repel each other. On the other hand, there are carbon atoms with opposite charges in the middle part of the helix, which create attractive $\pi-\pi$ stacking interactions. An interplay between these opposing forces allows the molecule to retain its helical shape and rigidness. These, together with coupling of vibrations of similar chromophores (e.g., C=C bonds), suggest the appearance of an intense VCD signal. Indeed, Figure 5 shows that trioxa[11]-helicene produces intense and rich VCD spectra.

Figure 6 compares the theoretically simulated (at the B3LYP/6-311++G(d,p) level of theory) IR and VCD spectra for the E2 enantiomer with the corresponding experimental spectra. Table 3 summarizes the most intense experimental and calculated IR and VCD bands and their assignments. As usual, the calculated wavenumbers are slightly overestimated at the high wavenumber range of the spectrum compared to the experiment, which can be improved by scaling. Overall good agreement between the calculated and experimental spectra both for IR (*Sim*IR = 0.80) and for VCD (*Sim*VCD = 0.71) (Table S1) demonstrates that the B3LYP level of theory is adequate for reproducing the vibrational chiroptical properties of such helicenes.

https://dx.doi.org/10.1021/acsomega.0c06079
ACS Omega 2021, 6, 2420−2428

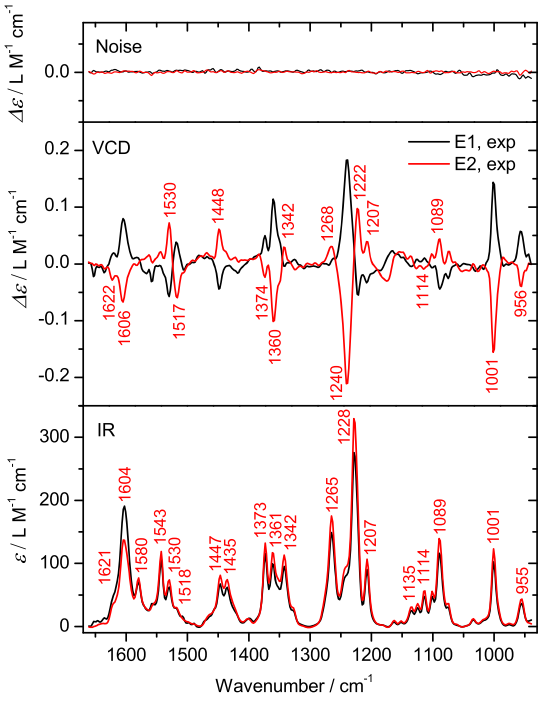

Figure 5. Experimental IR (bottom), VCD (middle), and noise (top) spectra of the E1 and E2 enantiomers measured in $CDCl_3$. The peak positions relate to E2.

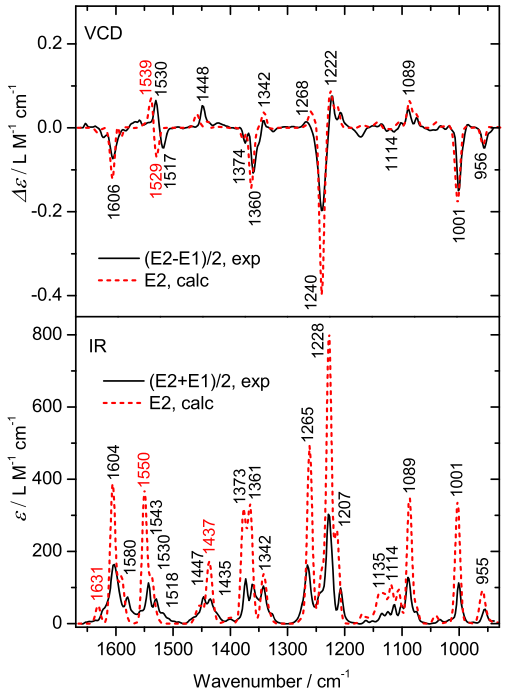

Figure 6. Experimental (measured in $CDCl_3$) and calculated (B3LYP/PCM($CHCl_3$)) IR (bottom) and VCD (top) spectra for the E2 enantiomer (black numbers - experiment, red - calculated). The calculated wavenumbers were multiplied by a scaling factor of 0.9867. Experimental spectra of the enantiomers were averaged using (E2 − E1)/2 (VCD) and (E2 + E1)/2 (IR).

The VCD spectra of the enantiomers represent the "mirror image" for most of the bands (Figure 5). The most intense IR and VCD signal appears between 1300 and 1200 cm^{-1} and originates from C−H in-plane bending, ring breathing, and C−O stretching modes (Table 3). The strongest IR band at 1228 cm^{-1} gives rise to the strongest nonconservative VCD couplet at 1240(−)/1222(+) cm^{-1} (Figures 5 and 6 and Table 3). The vibrational dissymmetry factor for this transition is quite large (VDF = 2.2 × 10^{-3}, Figure S3), reflecting a significant magnetic dipole contribution.

Similarly, a large dissymmetry factor (VDF = 1.4 × 10^{-3}) is observed for the VCD band measured at 1001 cm^{-1} and calculated at 1003 cm^{-1}, arising from the IR band at the same wavenumber and also coming from C−O stretching and ring breathing modes (Table 3). The region between 1150 and 1050 cm^{-1} shows only weak VCD features, coming from an overlay of multiple IR bands arising mainly from C−H in-plane bending and C−O stretching vibrations. A stronger but equally complex VCD signal is also observed in the region between 1400 and 1300 cm^{-1}, with the most intense negative band at 1360 cm^{-1}. These VCD intensities also come from the broad multicomponent IR band associated with coupled C−H in-plane bending and stretching of the bonds between five- and six-membered rings such as the bonds connecting R2/R3, R3/R4, R5/R6, R6/R7, R8/R9, and R9/R10. The VCD features in the higher-energy range between 1650 and 1400 cm^{-1} are relatively simpler and show well-defined negative or positive bands, mostly associated with the C−H in-plane bending and

Table 3. Experimental (Measured in $CDCl_3$) and Calculated (B3LYP/PCM($CHCl_3$)) IR Absorption and VCD Band Wavenumbers (cm^{-1}) for the E2 Enantiomer and Corresponding Band Assignments[a]

experimental		calculated		
IR	VCD	IR	VCD	assignment
1621	1622(−)	1631	1631(−)	ν (C−C) [R1,R11]
1604	1606(−)	1605	1606(−)	ν (C−C) [R_4−R_8]
1580	1583(−)	1591	1591(−)	
1543		1550		ν (C−C) + δ_{in} (C−H)
1530	1530(+)	1538	1539(+)	ν (C−C) + δ_{in} (C−H)
1518	1517(−)	1529	1529(−)	
1464sh		1462sh		δ_{in} (C−H) [R_1,R_2,R_{10},R_{11}]
1447	1448(+)	1453	1459(+)/ 1448(−)	δ_{in} (C−H) + ν (C−C)
1435		1437	1440(+)/ 1432(−)	
1373	1374(−)	1377	1377(−)	δ_{in}(C−H) + ν (C−C) [R_1,R_2,R_{10},R_{11}]
1361	1360(−)	1366	1372(+)/ 1363(−)	δ_{in} (C−H) + ν (C−C) [R_4−R_8]
1342	1342(+)	1342	1341(+)	δ_{in} (C−H)
1265	1268(+)	1261	1259(+)	ν (C−O) + $\delta_{in(Ring\ breathing)}$
1228	1240(−)/ 1222(+)	1228	1240(−)/ 1225(+)	δ_{in} (C−H) + ν (C−O)
1207	1207(+)	1214	1214(+)	δ_{in} (C−H) [R1−R11]
1135	1136(+)	1139	1142(+)	δ_{in} (C−H) [R_7,R_8,R_{10},R_{11}]
1114	1114(−)	1119	1119(−)	
1089	1089(+)	1087	1087(+)	δ_{in} (C−H) + ν (C−O)
1001	1001(−)	1003	1003(−)	ν (C−O) + $\delta_{in(Ring\ breathing)}$ [R_1,R_{11}]
955	956(−)	959	958(−)	δ_{out} (C−H) [R_4,R_5,R_7,R_8]

[a] ν − stretching, δ_{in} − in-plane bending, δ_{out} − out-of-plane bending, sh − shoulder. Calculated wavenumbers multiplied by a scaling factor of 0.9867 are listed.

https://dx.doi.org/10.1021/acsomega.0c06079
ACS Omega 2021, 6, 2420−2428

C−C stretching. Interestingly, the strongest IR band in that range at 1543 cm^{-1} is not optically active, not producing any measurable VCD signal. At the same time, weaker bands at 1530 and 1518 cm^{-1} appear to be much more active, resulting in distinct VCD bands of opposite sign at 1530 and 1517 cm^{-1}, respectively.

Overall, the calculations show that the strongest VCD signals come from C−H in-plane and out-of-plane bending modes due to strong vibrational coupling in the stacked helicene rings. This probably explains why an earlier reported VCD spectrum of a heptathiophene did not show such large dissymmetry factors as it did not contain hydrogen atoms within the helix.[44]

Raman Optical Activity. Because of a strong fluorescence band of trioxa[11]helicene within 400−550 nm, we were not able to obtain experimental ROA spectra. Therefore, we present only the calculated Raman and ROA spectra in Figure 7. As can be expected from complementary selection

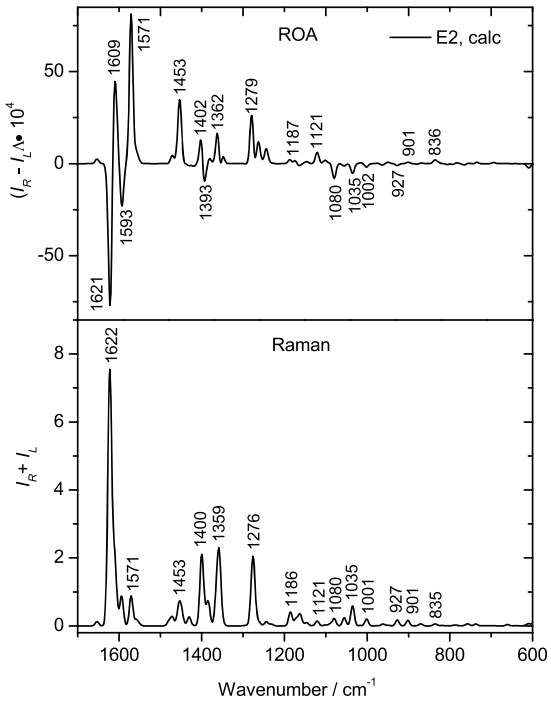

Figure 7. Calculated (B3LYP/PCM($CHCl_3$)) Raman and ROA spectra.

rules,[45−47] the most active region in IR and VCD between 1300 and 1000 cm^{-1} does not produce intense Raman or ROA bands. While IR/VCD require changes of the electric and magnetic dipole moments, typically associated with polar molecular parts, Raman/ROA intensities mostly originate in polarizability changes in aliphatic/aromatic residues. It has also been shown that IR-active bands are not so intense in Raman and vice versa.[45] For our molecule, the strongest ROA bands are calculated between 1700 and 1500 cm^{-1}. The most intense bands occur at 1621(−) and 1571(+) cm^{-1} and originate mainly from in-plane bending vibration, dominated by C−H bending.

CONCLUSIONS

We investigated the ECD, MCD, VCD, and ROA optical properties of one of the largest and relatively rigid helicenes that can be studied by computational methods at a high precision. Large dipole and magnetic moments together with strong coupling of the stacked helicene rings were identified as the most important factors contributing to the strong chiral response with maximal dissymmetry factors reaching 2×10^{-3} for VCD/ROA and 1×10^{-2} for ECD. MCD provided better resolution of the electronic transitions than ECD. The intense ECD bands are dominated by $\pi-\pi^*$ transitions, whereas those of VCD and ROA are dominated by in-plane and out-of-plane C−H bending vibrations. The B3LYP/6-311++G** method appeared as reasonably accurate and time-efficient for simulation of both the vibrational and electronic optical activities of the oxo-helicene. The sum-over-states (SOS) approach was found suitable to model the MCD intensities of helicenes.

METHODS

Chiral Separation. Trioxa[11]helicene was synthesized as described earlier.[30] The enantiomers were resolved by HPLC using a Chiralart Cellulose SC column (250 × 4.6 mm, 5 μm, YMC) and *n*-heptane/2-propanol (95:05) mixture as the mobile phase. The racemic sample was dissolved in *n*-heptane/2-propanol, injected in the chiral column, and detected with a UV detector at 254 nm. The earlier eluting fractions gave the enantiomer exhibiting positive optical rotation (+), which was isolated in 40% yield and nearly 100% enantiomeric excess (*ee*). Later eluting fractions consisted of the (−) enantiomer exhibiting negative optical rotation, in 42% yield and > 95% *ee*. The purity of both enantiomers was determined by chiral HPLC using the same stationary phase. Optical rotations of chloroform solutions were measured with an Autopol IV instrument (Rudolph Research Analytical) and found to be $[\alpha]_D^{25}$ +3803° (c = 0.160, $CHCl_3$) and −3610° (c = 0.154, $CHCl_3$) for the (+)-E1 (″*P*″) and (−)-E2 (″*M*″) isomers, respectively.

Spectral Measurements. The absorption and ECD spectra of nearly enantiomerically pure (>95% *ee*) samples were measured with a JASCO J-1500 spectrometer (Tokyo, Japan) in a range of 500−210 nm, using a quartz cuvette with a path length of 0.1 cm, scanning speed of 10 nm/min, and two spectra accumulations. MCD spectra were measured with a JASCO J-815 spectrometer (Tokyo, Japan), equipped with a permanent magnet (1.5 T), in two wavelength ranges: 340−230 nm (UV spectral range), using a 0.2 cm path length quartz cuvette, scanning speed of 10 nm/min, response time of 8 s; and 500−340 nm (visible spectral range), using a 0.5 cm path length quartz cuvette, scanning speed of 20 nm/min, and response time of 4 s; two spectral accumulations were averaged in both cases. The two setups were necessary to avoid strong absorption in the UV spectral range. The samples were dissolved in tetrahydrofuran (THF) at a concentration of 10^{-4} M for both ECD and MCD experiments. The spectrum of the pure solvent was subtracted as a baseline. MCD spectra were measured for both orientations of the magnet and obtained as a difference between the raw signal (composed of both MCD and ECD contributions) and ECD signal measured without the magnet.

For IR and VCD, both enantiomers were dissolved in deuterated chloroform ($CDCl_3$) (~14 mg/mL for E1 and ~16.5 mg/mL for E2) and contained in a sealed NaCl cell (PerkinElmer, USA) of 100 μm path length. $CDCl_3$ was used to avoid a spectral overlap with the strong $CHCl_3$ IR band around 1200 cm^{-1}. Both IR absorption and VCD spectra were

https://dx.doi.org/10.1021/acsomega.0c06079
ACS Omega 2021, 6, 2420−2428

measured simultaneously with a Fourier-transform Chiral IR-2X VCD spectrometer (BioTools, Inc., Jupiter, USA), in blocks of 1560 scans (~30 min) at 4 cm^{-1} resolution. 36 blocks were averaged to increase the signal-to-noise ratio. The solvent spectrum measured at the same conditions was subtracted from the sample spectra.

All the experimental spectral intensities were expressed in extinction coefficient (ε) units to allow for a direct comparison with the calculations.

Computations. DFT and TD-DFT calculations were performed using the B3LYP,[48−50] ωB97X-D,[41] and B3LYP-GD3 functionals together with Grimme's dispersion correction[51] and 6-311++G** basis set.[52] To mimic the environment, the integral equation polarizable continuum model (PCM)[53−55] with THF parameters was employed in absorption, ECD, and MCD calculations, while $CHCl_3$ parameters were used for calculations of IR, VCD, Raman, and ROA spectra. Vibrational (VCD, ROA) and TD-DFT[56] ECD calculations were performed at the same level of theory as the geometry optimization. 200 states were taken for TD-DFT. For the optimized geometries, no imaginary frequencies were observed. The calculations were performed using the Gaussian program package (version G16-A.03).[57] Mülliken atomic charges were used to support the $\pi-\pi$ stacking interaction analysis.

MCD intensities were calculated from the TD-DFT wave function obtained at the B3LYP/6-311++G**/PCM level of theory by applying the sum-over-states (SOS) approach.[58] As implemented in the GUVCDE program,[59,60] the SOS method uses configuration interaction coefficients and electronic energies provided in the Gaussian output. The SOS method provides results of the same quality as the coupled-perturbed approach[61] but allows treatment of larger molecules with a shorter computational time. An origin dependence of the results was avoided using the origin-independent localized orbital/local origin (LORG) method.[60]

Dissymmetry Factor Spectra and Similarity Analysis. Dissymmetry factor (DF) spectra were obtained as a ratio $g = \Delta\varepsilon/\varepsilon$.[46,62] Experimental and calculated electronic dissymmetry factor (EDF), magnetic dissymmetry factor (MDF), and vibrational dissymmetry factor (VDF) spectra are compared in Figures S1−S3, respectively. The regions with zero or near-zero intensities in the original spectra were not considered to avoid spike artifacts in DF spectra.

To quantitatively evaluate the agreement between the calculated and experimental spectra, we performed similarity analysis using the procedure described by Shen *et al.*[63] and Covington and Polavarapu.[62] The similarity analysis also allows determination of the optimal scaling factors maximizing the spectral similarity overlap. The similarity overlap values calculated for all the spectra studied along with the optimal scaling factors (if used) are given in Table S1. Note that similarity overlaps for DF spectra (*Sim*EDF, *Sim*MDF, and *Sim*VDF) are equivalent to *Sim*RAT as defined by Covington and Polavarapu.[62]

■ ASSOCIATED CONTENT

Supporting Information

The Supporting Information is available free of charge at https://pubs.acs.org/doi/10.1021/acsomega.0c06079.

Results of the similarity analysis; dissymmetry factor spectra; IR, VCD, Raman, and ROA spectra calculated using the ωB97X-D and B3LYP (with dispersion correction) functionals; PCM solvent effect ($CHCl_3$ vs THF) on the calculated spectra; Cartesian coordinates of the optimized structural models used in the calculations (PDF)

■ AUTHOR INFORMATION

Corresponding Authors

Taye B. Demissie − *Institute of Organic Chemistry and Biochemistry, Academy of Sciences, 16610 Prague, Czech Republic; Materials Science Program, Department of Chemistry, Addis Ababa University, Addis Ababa 1176, Ethiopia; Department of Chemistry, University of Botswana, 00704 Gaborone, Botswana;* orcid.org/0000-0001-8735-4933; Email: sene3095@gmail.com

Valery Andrushchenko − *Institute of Organic Chemistry and Biochemistry, Academy of Sciences, 16610 Prague, Czech Republic;* orcid.org/0000-0002-4874-0548; Email: valery.andrushchenko@uochb.cas.cz

Petr Bouř − *Institute of Organic Chemistry and Biochemistry, Academy of Sciences, 16610 Prague, Czech Republic;* orcid.org/0000-0001-8469-1686; Email: bour@uochb.cas.cz

Authors

M. Shyam Sundar − *Institute of Organic Chemistry and Biochemistry, Academy of Sciences, 16610 Prague, Czech Republic*

Karthick Thangavel − *Institute of Organic Chemistry and Biochemistry, Academy of Sciences, 16610 Prague, Czech Republic; Department of Physics, School of Electrical and Electronics Engineering, SASTRA Deemed University, Thanjavur 613 401, Tamil Nadu, India;* orcid.org/0000-0001-6029-8644

Ashutosh V. Bedekar − *Department of Chemistry, Faculty of Science, The Maharaja Sayajirao University of Baroda, Vadodara 390 002, India;* orcid.org/0000-0001-7537-5390

Complete contact information is available at: https://pubs.acs.org/10.1021/acsomega.0c06079

Notes

The authors declare no competing financial interest.

■ ACKNOWLEDGMENTS

This work was supported by the European Regional Development Fund, OP RDE, Project: "Chemical biology for drugging undruggable targets (ChemBioDrug)" (No. CZ.02.1.01/0.0/0.0/16_019/0000729), European Regional Development Fund, OP RDE, Project: "IOCB Mobility" (No. CZ.02.2.69/0.0/0.0/16_027/0008477), and the Czech Science Foundation (grant 18-05770S). Computer time was provided by CERIT-SC (CERIT Scientific Cloud) of the Czech Republic. We acknowledge Lucie Bednárová for measuring the ECD and MCD spectra of our sample at the IOCB instrument facility.

■ REFERENCES

(1) Gingras, M. One hundred years of helicene chemistry. Part 3: applications and properties of carbohelicenes. *Chem. Soc. Rev.* **2013**, *42*, 1051−1095.

(2) Shen, Y.; Chen, C.-F. Helicenes: Synthesis and Applications. *Chem. Rev.* **2012**, *112*, 1463−1535.

(3) Kim, C.; Marks, T. J.; Facchetti, A.; Schiavo, M.; Bossi, A.; Maiorana, S.; Licandro, E.; Todescato, F.; Toffanin, S.; Muccini, M.; Graiff, C.; Tiripicchio, A. Synthesis, characterization, and transistor response of tetrathia-[7]-helicene precursors and derivatives. *Org. Electron.* **2009**, *10*, 1511−1520.
(4) Martin, R. H. The Helicenes. *Angew. Chem., Int. Ed. Engl.* **1974**, *13*, 649−660.
(5) Yamada, K.-i.; Nakagawa, H.; Kawazura, H. Thermal Racemization of Thiaheterohelicenes. *Bull. Chem. Soc. Jpn.* **1986**, *59*, 2429−2432.
(6) Severa, L.; Adriaenssens, L.; Vávra, J.; Šaman, D.; Císařová, I.; Fiedler, P.; Teplý, F. Highly modular assembly of cationic helical scaffolds: rapid synthesis of diverse helquats via differential quaternization. *Tetrahedron* **2010**, *66*, 3537−3552.
(7) Hafedh, N.; Aloui, F.; Dorcet, V.; Barhoumi, H. Helically chiral functionalized [6]helicene: Synthesis, optical resolution, and photophysical properties. *C. R. Chim.* **2018**, *21*, 652−658.
(8) Tanaka, K.; Fukawa, N.; Suda, T.; Noguchi, K. One-Step Construction of Five Successive Rings by Rhodium-Catalyzed Intermolecular Double [2+2+2] Cycloaddition: Enantioenriched [9]Helicene-Like Molecules. *Angew. Chem., Int. Ed.* **2009**, *48*, 5470−5473.
(9) Rajca, A.; Wang, H.; Pink, M.; Rajca, S. Annelated Heptathiophene: A Fragment of a Carbon−Sulfur Helix. *Angew. Chem., Int. Ed.* **2000**, *39*, 4481−4483.
(10) Hoffmann, R.; Hopf, H. Learning from Molecules in Distress. *Angew. Chem., Int. Ed.* **2008**, *47*, 4474−4481.
(11) Zhang, X.; Clennan, E. L.; Petek, T.; Weber, J. Synthesis, computational, and photophysical characterization of diaza-embedded [4]helicenes and pseudo[4]helicenes and their pyridinium and viologen homologues. *Tetrahedron* **2017**, *73*, 508−518.
(12) Gingras, M.; Félix, G.; Peresutti, R. One hundred years of helicene chemistry. Part 2: stereoselective syntheses and chiral separations of carbohelicenes. *Chem. Soc. Rev.* **2013**, *42*, 1007−1050.
(13) Gingras, M. One hundred years of helicene chemistry. Part 1: non-stereoselective syntheses of carbohelicenes. *Chem. Soc. Rev.* **2013**, *42*, 968−1006.
(14) Mitsui, C.; Soeda, J.; Miwa, K.; Tsuji, H.; Takeya, J.; Nakamura, E. Naphtho[2,1-b:6,5-b′]difuran: A Versatile Motif Available for Solution-Processed Single-Crystal Organic Field-Effect Transistors with High Hole Mobility. *J. Am. Chem. Soc.* **2012**, *134*, 5448−5451.
(15) Tsuji, H.; Mitsui, C.; Ilies, L.; Sato, Y.; Nakamura, E. Synthesis and Properties of 2,3,6,7-Tetraarylbenzo[1,2-b:4,5-b′]difurans as Hole-Transporting Material. *J. Am. Chem. Soc.* **2007**, *129*, 11902−11903.
(16) Wang, X.-Y.; Wang, X.-C.; Narita, A.; Wagner, M.; Cao, X.-Y.; Feng, X.; Müllen, K. Synthesis, Structure, and Chiroptical Properties of a Double [7]Heterohelicene. *J. Am. Chem. Soc.* **2016**, *138*, 12783−12786.
(17) Newman, M. S.; Darlak, R. S.; Tsai, L. L. Optical properties of hexahelicene. *J. Am. Chem. Soc.* **1967**, *89*, 6191−6193.
(18) Grimme, S.; Harren, J.; Sobanski, A.; Vögtle, F. Structure/Chiroptics Relationships of Planar Chiral and Helical Molecules. *Eur. J. Org. Chem.* **1998**, 1491−1509.
(19) Grimme, S. Calculation of the electronic spectra of large molecules. *Rev. Comput. Chem.* **2004**, *20*, 153−218.
(20) Botek, E.; Champagne, B. Circular dichroism of helical structures using semiempirical methods. *J. Chem. Phys.* **2007**, *127*, 204101.
(21) Bannwarth, C.; Seibert, J.; Grimme, S. Electronic Circular Dichroism of [16]Helicene With Simplified TD-DFT: Beyond the Single Structure Approach. *Chirality* **2016**, *28*, 365−369.
(22) Magyarfalvi, G.; Tarczay, G.; Vass, E. Vibrational circular dichroism. *WIREs Comput. Mol. Sci.* **2011**, *1*, 403−425.
(23) Parchaňský, V.; Kapitán, J.; Bouř, P. Inspecting chiral molecules by Raman optical activity spectroscopy. *RSC Adv.* **2014**, *4*, 57125−57136.
(24) Abbate, S.; Lebon, F.; Longhi, G.; Fontana, F.; Caronna, T.; Lightner, D. A. Experimental and calculated vibrational and electronic circular dichroism spectra of 2-Br-hexahelicene. *Phys. Chem. Chem. Phys.* **2009**, *11*, 9039−9043.
(25) Berova, N.; Polavarapu, P.; Nakanishi, H.; Woody, R. W. W. *Comprehensive Chiroptical Spectroscopy: Instrumentation, Methodologies, and Theoretical Simulations*; John Wiley & Sons, Inc.: Hoboken, New Jersey, United States, 2011.
(26) Bürgi, T.; Urakawa, A.; Behzadi, B.; Ernst, K.-H.; Baiker, A. The absolute configuration of heptahelicene: aVCD spectroscopy study. *New J. Chem.* **2004**, *28*, 332−334.
(27) Mobian, P.; Nicolas, C.; Francotte, E.; Bürgi, T.; Lacour, J. Synthesis, Resolution, and VCD Analysis of an Enantiopure Diazaoxatricornan Derivative. *J. Am. Chem. Soc.* **2008**, *130*, 6507−6514.
(28) Shen, C.; Srebro-Hooper, M.; Weymuth, T.; Krausbeck, F.; Navarrete, J. T. L.; Ramírez, F. J.; Nieto-Ortega, B.; Casado, J.; Reiher, M.; Autschbach, J.; Crassous, J. Redox-Active Chiroptical Switching in Mono- and Bis-Iron Ethynylcarbo[6]helicenes Studied by Electronic and Vibrational Circular Dichroism and Resonance Raman Optical Activity. *Chem. − Eur. J.* **2018**, *24*, 15067−15079.
(29) Nakai, Y.; Mori, T.; Inoue, Y. Circular Dichroism of (Di)methyl- and Diaza[6]helicenes. A Combined Theoretical and Experimental Study. *J. Phys. Chem. A* **2013**, *117*, 83−93.
(30) Shyam Sundar, M.; Bedekar, A. V. Synthesis and Study of 7,12,17-Trioxa[11]helicene. *Org. Lett.* **2015**, *17*, 5808−5811.
(31) Stephens, P. J. Magnetic Circular Dichroism. *Annu. Rev. Phys. Chem.* **1974**, *25*, 201−232.
(32) Stephens, P. J. Theory of Magnetic Circular Dichroism. *J. Chem. Phys.* **1970**, *52*, 3489−3516.
(33) Štěpánek, P.; Straka, M.; Andrushchenko, V.; Bouř, P. Fullerene resolution by the magnetic circular dichroism. *J. Chem. Phys.* **2013**, *138*, 151103.
(34) Štěpánek, P.; Straka, M.; Šebestík, J.; Bouř, P. Magnetic circular dichroism of chlorofullerenes: Experimental and computational study. *Chem. Phys. Lett.* **2016**, *647*, 117−121.
(35) Kaminský, J.; Chalupský, J.; Štěpánek, P.; Kříž, J.; Bouř, P. Vibrational Structure in Magnetic Circular Dichroism Spectra of Polycyclic Aromatic Hydrocarbons. *J. Phys. Chem. A* **2017**, *121*, 9064−9073.
(36) Furche, F.; Ahlrichs, R.; Wachsmann, C.; Weber, E.; Sobanski, A.; Vögtle, F.; Grimme, S. Circular Dichroism of Helicenes Investigated by Time-Dependent Density Functional Theory. *J. Am. Chem. Soc.* **2000**, *122*, 1717−1724.
(37) Nakai, Y.; Mori, T.; Inoue, Y. Theoretical and Experimental Studies on Circular Dichroism of Carbo[n]helicenes. *J. Phys. Chem. A* **2012**, *116*, 7372−7385.
(38) Johannessen, C.; Blanch, E. W.; Villani, C.; Abbate, S.; Longhi, G.; Agarwal, N. R.; Tommasini, M.; Lightner, D. A. Raman and ROA Spectra of (−)- and (+)-2-Br-Hexahelicene: Experimental and DFT Studies of a π-Conjugated Chiral System. *J. Phys. Chem. B* **2013**, *117*, 2221−2230.
(39) Furche, F.; Ahlrichs, R. Adiabatic time-dependent density functional methods for excited state properties. *J. Chem. Phys.* **2002**, *117*, 7433−7447.
(40) Isla, H.; Saleh, N.; Ou-Yang, J.-K.; Dhbaibi, K.; Jean, M.; Dziurka, M.; Favereau, L.; Vanthuyne, N.; Toupet, L.; Jamoussi, B.; Srebro-Hooper, M.; Crassous, J. Bis-4-aza[6]helicene: A Bis-helicenic 2,2′-Bipyridine with Chemically Triggered Chiroptical Switching Activity. *J. Org. Chem.* **2019**, *84*, 5383−5393.
(41) Chai, J.-D.; Head-Gordon, M. Long-range corrected hybrid density functionals with damped atom−atom dispersion corrections. *Phys. Chem. Chem. Phys.* **2008**, *10*, 6615−6620.
(42) Hudecová, J.; Profant, V.; Novotná, P.; Baumruk, V.; Urbanová, M.; Bouř, P. CH Stretching Region: Computational Modeling of Vibrational Optical Activity. *J. Chem. Theory Comput.* **2013**, *9*, 3096−3108.
(43) Miyasaka, M.; Pink, M.; Rajca, S.; Rajca, A. Noncovalent Interactions in the Asymmetric Synthesis of Rigid, Conjugated Helical Structures. *Angew. Chem., Int. Ed.* **2009**, *48*, 5954−5957.

https://dx.doi.org/10.1021/acsomega.0c06079
ACS Omega 2021, 6, 2420−2428

(44) Freedman, T. B.; Cao, X.; Rajca, A.; Wang, H.; Nafie, L. A. Determination of Absolute Configuration in Molecules with Chiral Axes by Vibrational Circular Dichroism: A C_2-Symmetric Annelated Heptathiophene and a D_2-Symmetric Dimer of 1,1'-Binaphthyl. *J. Phys. Chem. A* **2003**, *107*, 7692−7696.
(45) Andrushchenko, V.; Benda, L.; Páv, O.; Dračínský, M.; Bouř, P. Vibrational Properties of the Phosphate Group Investigated by Molecular Dynamics and Density Functional Theory. *J. Phys. Chem. B* **2015**, *119*, 10682−10692.
(46) Barron, L. D. *Molecular Light Scattering and Optical Activity*; 2 ed.; Cambridge University Press: Cambridge, 2009.
(47) Nafie, L. A. *Vibrational Optical Activity: Principles and Applications*; John Wiley & Sons, Ltd: Chichester, 2011, DOI: 10.1002/9781119976516.
(48) Becke, A. D. Density-functional thermochemistry. III. The role of exact exchange. *J. Chem. Phys.* **1993**, *98*, 5648−5652.
(49) Lee, C.; Yang, W.; Parr, R. G. Development of the Colle-Salvetti correlation-energy formula into a functional of the electron density. *Phys. Rev. B* **1988**, *37*, 785−789.
(50) Stephens, P. J.; Devlin, F. J.; Chabalowski, C. F.; Frisch, M. J. Ab Initio Calculation of Vibrational Absorption and Circular Dichroism Spectra Using Density Functional Force Fields. *J. Phys. Chem.* **1994**, *98*, 11623−11627.
(51) Grimme, S. Density functional theory with London dispersion corrections. *WIREs Comput. Mol. Sci.* **2011**, *1*, 211−228.
(52) Krishnan, R.; Binkley, J. S.; Seeger, R.; Pople, J. A. Self-Consistent Molecular Orbital Methods. XX. A Basis Set for Correlated Wave Functions. *J. Chem. Phys.* **1980**, *72*, 650−654.
(53) Cancès, E.; Mennucci, B.; Tomasi, J. A New Integral Equation Formalism for the Polarizable Continuum Model: Theoretical Background and Applications to Isotropic and Anisotropic Dielectrics. *J. Chem. Phys.* **1997**, *107*, 3032−3041.
(54) Mennucci, B.; Tomasi, J. Continuum Solvation Models: A New Approach to The Problem of Solute's Charge Distribution and Cavity Boundaries. *J. Chem. Phys.* **1997**, *106*, 5151−5158.
(55) Tomasi, J.; Mennucci, B.; Cammi, R. Quantum Mechanical Continuum Solvation Models. *Chem. Rev.* **2005**, *105*, 2999−3094.
(56) Grimme, S.; Furche, F.; Ahlrichs, R. An improved method for density functional calculations of the frequency-dependent optical rotation. *Chem. Phys. Lett.* **2002**, *361*, 321−328.
(57) Frisch, M. J.; Trucks, G. W.; Schlegel, H. B.; Scuseria, G. E.; Robb, M. A.; Cheeseman, J. R.; Montgomery, Jr., J. A.; Vreven, T.; Kudin, K. N.; Burant, J. C.; Millam, J. M.; Lyengar, S. S.; Tomasi, J.; Barone, V.; Mennucci, B.; Cossi, M.; Scalmani, G.; Rega, N.; Petersson, G. A.; Nakatsuji, H.; Hada, M.; Ehara, M.; Toyota, K.; Fukuda, R.; Hasegawa, J.; Ishida, M.; Nakajima, T.; Honda, Y.; Kitao, O.; Nakai, H.; Klene, M.; Li, X.; Knox, J. E.; Hratchian, H. P.; Cross, J. B.; Bakken, V.; Adamo, C.; Jaramillo, J.; Gomperts, R.; Stratmann, R. E.; Yazyev, O.; Austin, A. J.; Cammi, R.; Pomelli, C.; Ochterski, J. W.; Ayala, P. Y.; Morokuma, K.; Voth, G. A.; Salvador, P.; Dannenberg, J. J.; Zakrzewski, V. G.; Dapprich, S.; Daniels, A. D.; Strain, M. C.; Farkas, O.; Malick, D. K.; Rabuck, A. D.; Raghavachari, K.; Foresman, J. B.; Ortiz, J. V.; Cui, Q.; Baboul, A. G.; Clifford, S.; Cioslowski, J.; Stefanov, B. B.; Liu, G.; Liashenko, A.; Piskorz, P.; Komaromi, I.; Martin, R. L.; Fox, D. J.; Keith, T.; Al-Laham, M. A.; Peng, C. Y.; Nanayakkara, A.; Challacombe, M.; Gill, P. M. W.; Johnson, B.; Chen, W.; Wong, M. W.; Gonzalez, C.; Pople, J. A. *Gaussian 16*; Revision A.03 ed.; Gaussian, Inc.: Wallingford CT, 2016.
(58) Autschbach, J.; Seth, M.; Ziegler, T. Development of a sum-over-states density functional theory for both electric and magnetic static response properties. *J. Chem. Phys.* **2007**, *126*, 174103.
(59) Randaccio, L.; Furlan, M.; Geremia, S.; Šlouf, M.; Srnova, I.; Toffoli, D. Similarities and Differences between Cobalamins and Cobaloximes. Accurate Structural Determination of Methylcobalamin and of LiCl- and KCl-Containing Cyanocobalamins by Synchrotron Radiation. *Inorg. Chem.* **2000**, *39*, 3403−3413.
(60) Štěpánek, P.; Bouř, P. Origin-Independent Sum Over States Simulations of Magnetic and Electronic Circular Dichroism Spectra via the Localized Orbital/Local Origin Method. *J. Comput. Chem.* **2015**, *36*, 723−730.
(61) Ghidinelli, S.; Abbate, S.; Mazzeo, G.; Paoloni, L.; Viola, E.; Ercolani, C.; Donzello, M. P.; Longhi, G. Characterization of Tetrakis(Thiadiazole)Porphyrazine Metal Complexes by Magnetic Circular Dichroism and Magnetic Circularly Polarized Luminescence. *Chirality* **2020**, *32*, 808−816.
(62) Covington, C. L.; Polavarapu, P. L. Similarity in Dissymmetry Factor Spectra: A Quantitative Measure of Comparison between Experimental and Predicted Vibrational Circular Dichroism. *J. Phys. Chem. A* **2013**, *117*, 3377−3386.
(63) Shen, J.; Zhu, C.; Reiling, S.; Vaz, R. A novel computational method for comparing vibrational circular dichroism spectra. *Spectrochim. Acta, Part A* **2010**, *76*, 418−422.

https://dx.doi.org/10.1021/acsomega.0c06079
ACS Omega 2021, 6, 2420−2428